Earth and Planetary Science Letters 470 (2017) 37–47

Contents lists available at ScienceDirect

Earth and Planetary Science Letters

www.elsevier.com/locate/epsl

The percolation threshold and permeability evolution of ascending magmas

Alain Burgisser [a,*], Laure Chevalier [a], James E. Gardner [b], Jonathan M. Castro [c]

[a] Univ. Savoie Mont Blanc, CNRS, IRD, ISTerre, F-73376 Le Bourget du Lac, France
[b] Department of Geological Sciences, The University of Texas at Austin, Austin, TX 78712-0254, USA
[c] Institute of Geosciences, Johannes Gutenberg University Mainz, Mainz, Germany

ARTICLE INFO

Article history:
Received 5 November 2016
Received in revised form 11 April 2017
Accepted 12 April 2017
Available online xxxx
Editor: T.A. Mather

Keywords:
rhyolite
experimental petrology
conduit flow
volcanic eruption

ABSTRACT

The development of gas permeability in magmas is a complex phenomenon that directly influences the style of a volcanic eruption. The emergence of permeability is linked to the concept of percolation threshold, which is the point beyond which gas bubbles are connected in a continuous network that allows gas escape. Measurements of the percolation threshold, however, range from ~30 to 78 vol%. No known combination of parameters can explain such a wide range of threshold values, which affects our understanding of the relationship between percolation and permeability. We present permeability calculations on bubble-bearing rhyolitic melts that underwent experimental decompression. Samples were analyzed by X-ray microtomography to image the bubble networks in 3D. We develop a percolation threshold for magmas that depends on the bubble network characteristics of this sample set. This relationship recovers the behavior of a wide range of volcanic samples by separating permeable samples from impermeable ones with a success rate of 88%. We use this percolation threshold to propose simplified permeability relationships that rely on parameters widely used in numerical modeling of magma flow. These relationships are valid within one order of magnitude for the viscous permeability coefficient and within two orders of magnitude for the inertial coefficient. They recover the ranges of values previously covered by isolated relationships, reassembling them within a single framework. We test the implications of such unification on eruptive dynamics with a 1D, two-phase conduit flow model. This test shows that varying the percolation threshold has little influence on vertical gas loss and ascent dynamics.

1. Introduction

During a volcanic eruption, magma ascends towards the surface and loses the volatiles it contains. In viscous magmas, volatiles are lost as gas bubbles that grow during ascent but hardly move relative to each other. The coalescence of the bubbles with each other transforms the bubbly magma into a connected network that is permeable to gas (e.g., Eichelberger et al., 1986). Permeability allows the gas to separate from the magma (e.g., Yoshida and Koyaguchi, 1999). An efficient separation promotes effusive eruptions, whereas bubble accumulation by growth promotes fragmentation and explosive eruptions (e.g., Jaupart and Allègre, 1991).

Studies aimed at understanding magma permeability have established relationships that depend on material properties, such as bubble size, total and connected gas volume fraction, throat size (aperture of inter-bubble connections), bubble aspect ratio, and network tortuosity (Klug and Cashman, 1996; Mueller et al., 2005; Wright et al., 2009; Yokoyama and Takeuchi, 2009; Degruyter et al., 2010a). Focusing on natural data, permeability relationships went from the apparent simplicity of depending only on total gas volume fraction (Klug and Cashman, 1996) to larger degrees of complexity as more data were acquired and more degrees of freedom were needed to describe the relationships (Saar and Manga, 1999). Another degree of complexity was reached when a second permeability coefficient was introduced alongside the original coefficient entering Darcy's law. While the first permeability coefficient, k_1, quantifies the effects of gas flow when viscous effects dominate, the additional coefficient, k_2, takes into account the inertial effects of turbulent flow (Rust and Cashman, 2004). It was also found that the relationships gain in accuracy of permeability prediction when using connected gas volume fraction instead of total gas fraction (Saar and Manga, 1999; Mueller et al., 2005; Gonnermann and Manga, 2007). The relationship between total and connected porosity is directly linked to the threshold at which

* Corresponding author. Fax: +33 479 758 742
E-mail address: alain.burgisser@univ-savoie.fr (A. Burgisser).

http://dx.doi.org/10.1016/j.epsl.2017.04.023
0012-821X/

Table 1
Symbol list. The mean bubble diameter is based on the diameter distribution and the average bubble diameter is based on volume distribution (see Methods).

Symbol	Description (unit)
A	Proportionality constant
a_i	Semi-axes of ellipsoid (m)
a_{KC}	Constant in Kozeny–Carman equation (m^2)
a_M	Constant in percolation equation (m^2)
B	Proportionality constant
b_{KC}	Exponent in Kozeny–Carman equation
b_M	Exponent in percolation equation
c_d	Percolation constant (m)
c_ϕ	Connected porosity constant
c_p	Connected porosity constant (m)
c_τ	Tortuosity constant
c_z	Percolation exponent
χ_i	Bubble aspect ratio
d_a	Average bubble diameter (m)
d_m	Mean bubble diameter (m)
d_t	Throat diameter (m)
ε_i	Bubble elongation
f_0	Inertial factor
ϕ_c	Connected porosity
ϕ_p	Percolation porosity
ϕ_t	Total porosity
i, k	Indices of spatial direction
k_1	Viscous permeability (m^2)
k_2	Inertial permeability (m)
l_i	Longest semi-axis of ellipsoid orthogonal to i (m)
m	Exponent in Archie's law
μ	Fluid viscosity (Pa s)
n	Exponent in Degruyter equation
N_m	Bubble number density per unit melt (m^{-3})
P	Pressure (Pa)
ρ	Fluid density (kg/m^3)
r_i	Radius of equivalent disk of ellipsoid cross-section orthogonal to i (m)
R_1, R_2, R_3	Sum of residuals
σ_a	Standard deviation of d_a (m)
σ_m	Standard deviation of d_m (m)
τ_i	Tortuosity
v_i	Fluid velocity (m/s)
$\vec{w}$	Vector of components a_i
x_i	Spatial direction
z	Calculated inter-bubble distance (m)
z_m	Measured inter-bubble distance (m)
Z	Scaled inter-bubble distance (m)
Z_p	Percolation threshold on Z (m)

the magma ceases to be impermeable to gas. Drawing from percolation theory (Sahini and Sahimi, 1994), this threshold has mostly been assumed to depend on a constant value of gas volume fraction (Blower, 2001). Characterizing the percolation threshold in natural products (e.g., Eichelberger et al., 1986; Klug and Cashman, 1996; Saar and Manga, 1999; Mueller et al., 2005), experimental magmas (e.g., Takeuchi et al., 2009; Martel and Iacono-Marziano, 2015), and analogue materials (e.g, Namiki and Manga, 2008) led to values ranging from ~30 to 78 vol%. Several possible controls of such a wide range of values have been proposed: crystal volume fraction, melt viscosity, shear stress, decompression rate, differences in experimental methodology, and the inaccuracy of theoretical models that do not take into account the time needed for interstitial film retraction (Okumura et al., 2013; Rust and Cashman, 2011; Lindoo et al., 2016). Some parameters, such as shear stress, give a partial explanation for the variability of measured percolation thresholds (Caricchi et al., 2011; Okumura et al., 2013), whereas others, such as melt viscosity, do not seem to control this variability (Lindoo et al., 2016). None explain the full spectrum of threshold values.

The transition of magma from being permeable to impermeable controls when gas escape ceases. The amount of gas escape, on the other hand, is controlled by permeability, which directly influences the style of the volcanic eruption (Yoshida and Koyaguchi, 1999; Kozono and Koyaguchi, 2009; Degruyter et al., 2012). Clarifying the relationship between percolation and permeability is thus an important issue.

Here we investigate the role of the bubble network geometry on the percolation threshold and on permeability. (See Table 1.) We use a subset of two series of experiments (Burgisser and Gardner, 2004; Gardner, 2007) on silicate melts in which bubbles grew during isothermal decompression and interacted to various degrees, sometimes creating a permeable network by coalescence. These crystal-free experiments were analyzed by X-ray Computed Tomography (CT) to obtain 3D reconstructions of the bubble networks, as described in Castro et al. (2012). Bubble network parameters and both viscous and inertial permeability coefficients were calculated so as to test the relationship of Degruyter et al. (2010a) against our data set. That relationship assumes that the state of percolation and network parameters are known. We relax these assumptions by making the relationships depend on 1) a percolation threshold related to bubble network geometry and 2) magmatic parameters widely used in conduit flow models. We establish that the percolation depends on bubble separation and on the degree of polydispersity of the bubble size distribution. The resulting relationship links inertial and viscous permeabilities to the average and standard deviation of the bubble size distribution, bubble aspect ratio, and total porosity. We show how the proposed percolation threshold captures the behavior of previously published data sets. Finally, we explore some implications of having a unified framework predicting magma permeability on conduit flow model outputs.

2. Methods

2.1. CT volumes

We analyzed a subset of 36 samples from experimentally decompressed rhyolite melts. Briefly, the Burgisser and Gardner (2004) and the Gardner (2007) experiments consisted of placing samples of rhyolitic glass in sealed Au-capsules with distilled water, and equilibrating them at 150 MPa for five days in order to saturate the melt with water. Some capsules were quenched, removed from the pressure vessel, and opened to extract the hydrated samples. These samples were reloaded into Au capsules without water, but with either silicate glass powder or MgO powder to serve as a sink for expelled water during decompression, allowing open-degassing conditions. Each capsule was then repressurized and reheated at the hydration conditions for 5 min before an applied sudden decompression nucleated small bubbles (mean radius $<<$10 μm). The other samples – i.e. those that had not been reopened and reloaded – remained in the pressure vessel until the nucleation step was performed, thus ensuring closed-system conditions. All samples were maintained at the nucleation pressure until bubbles reached thermodynamic equilibrium, which was checked by determining the glass water content (Gardner, 2007). Pressure was then released in increments to approximate a constant decompression rate until a final pressure was reached, at which samples were quenched rapidly.

All volumes analyzed by CT (Castro et al., 2012) come from hydrated and foamed cores that underwent decompression in either closed, or open degassing conditions. These samples were sometimes small pieces broken from the original cores and sometimes were parts of thin sections that were recut with a diamond saw so as to leave the smallest possible amount of thin section glass attached to the sample. As a result, while the former samples are often equant and yielded nearly cubic CT volumes, the latter samples were much thinner in one direction and yielded highly flattened volumes (details in Supplementary Text S1 and Fig. S1).

Connected bubbles have retained their original shapes. When these shapes are mostly spherical, we refer to the sample as be-

ing isotropic. Some volumes contain ellipsoidal bubbles. They come from the top part of hydrated and foamed samples and we refer to these samples as being anisotropic. Sample deformation is likely due to volumetric expansion of the sample during decompression that forced the melt in the crimped ends of the capsule (Burgisser and Gardner, 2004). In these deformed areas, both bubble elongation amplitude and direction vary significantly. CT volumes were selected so that bubbles have clearly visible and homogeneous orientation fabric. These anisotropic samples were rotated so that the principal directions of elongation correspond to those of the sample edges (x, y and z axes).

2.2. Bubble network parameters

The CT volumes were digitally thresholded in order to distinguish bubbles from glass. Some samples contain <1 vol.% of Fe–Ti oxides, which were grouped with the glass category. The software ImageJ (version 1.49) and associated plugins were used to quantify the three-dimensional network of bubbles. Bubbles are not distributed homogeneously in space. The distance separating two neighboring bubbles is thus best measured by focusing on the glass phase. Bubble separation distance, z_m, is the mean value given by the "Thickness" plugin of the BoneJ (version 1.3.11) bundle (Doube et al., 2010), which measures at each voxel of the glass phase the diameter of the largest sphere that fits within the glass phase and that contains that voxel. Connected porosity was measured by adding all the connected volumes given by the "3D object counter" plugin (Bolte and Cordelières, 2006) that had bounding boxes as large as the CT volume (i.e. that span the volume from side to side). In most samples, bubbles form an interconnected network. Original bubbles can nevertheless be separated because they connect to each other by narrow throats (Supplementary Text S1 and Fig. S2). The software Blob3D (Ketcham, 2005) was used to separate bubbles either by erosion or planar cut. Bubble and throat shapes were measured for the whole sample whenever possible. When the number of bubbles in the CT volume was too large to be fully analyzed with Blob3D, a representative sub-volume was used to determine bubble and throat shape statistics. Throat diameter, d_t, was defined as the diameter of the disk equivalent to the measured throat surface. The throat diameter value used for calculation is the median for the sample and the standard deviation gives the spread of this parameter. Bubble number density with respect to melt volume, N_m, was calculated using the total number of counted bubbles in the sample volume, except for samples where the total number of bubbles was not fully counted. Instead, N_m for those samples are the total bubble number densities reported in Burgisser and Gardner (2004) and Gardner (2007), corrected for sample porosity.

Bubble diameter, d_a, was calculated as the diameter of the equivalent sphere corresponding to the average bubble volume, which is the sum of all bubble volumes divided by the number of bubbles. The uncertainty on bubble diameter, σ_a, corresponds to half the difference between the 16th and 84th percentile of the volume distribution. This measure of standard deviation takes into account that the shape distribution spans from Gaussian to power law (Burgisser and Gardner, 2004). Most studies on bubble size distributions have used the mean bubble diameter, d_m, instead of d_a as the characteristic bubble diameter (e.g., Burgisser and Gardner, 2004; Takeuchi et al., 2009; Bai et al., 2010). We found that d_a yields generally better fits with the permeability relationships we consider herein. Formally, d_a corresponds to the ratio between the 4th and 3rd moments of the bubble diameter distribution, and d_m is the arithmetic mean of the distribution. This ratio fits our measurements, but it needs the full size distribution to convert d_m into d_a. Because most studies report only d_m, and its associated standard deviation, σ_m, we instead use empirical relationships that depend only on these two quantities to retrieve d_a from the published d_m:

$$d_a = A d_m \left(1 + \frac{\sigma_m}{d_m}\right) \tag{1}$$

$$\sigma_a = AB\sigma_m \left(1 + \frac{\sigma_m}{d_m}\right) \tag{2}$$

These relations fit very well with our measurements when the proportionality constants, A and B, are set to 0.87 and 0.64, respectively. We use the ratio of σ_a to d_a as a measure of the degree of polydispersity of the distribution: $\sigma_a/d_a = B\sigma_m/d_m$.

Some permeability relationships involve a cross-section shape factor, χ_i (Degruyter et al., 2010a):

$$\chi_i = \left(\frac{l_i^2}{r_i^2} + \frac{r_i^2}{l_i^2}\right) \tag{3}$$

where l_i is the longest semi-axis of the ellipsoid cross-section area orthogonal to direction i and r_i is the radius of the equivalent disk of the ellipsoid cross-section area. Because the anisotropic samples were oriented so that the bubble major axes of elongation match the sample edge directions, we define a_i as the semi-axes of the Blob3D best-fit ellipsoids of the bubbles. We assume that l_i corresponds to the maximum of the ellipsoid semi-axes orthogonal to the selected direction i with $k = x, y, z$:

$$l_i = max(a_{k,k\neq i}) \tag{4}$$

The parameter r_i is:

$$r_i = \sqrt{\prod (a_{k,k\neq i})} \tag{5}$$

Equation (3) thus becomes:

$$\chi_i = \left(\frac{max(a_{k,k\neq i})}{min(a_{k,k\neq i})} + \frac{min(a_{k,k\neq i})}{max(a_{k,k\neq i})}\right) \tag{6}$$

Cross-section shape factors were calculated in three directions of space for each bubble in a given sample. The χ_i values of each sample correspond to the median values over all the bubbles. The single χ value of isotropic samples was averaged over the three directions of space.

The parameter ε_i is a measure of the bubble relative elongation in direction i. Considering the vector $\vec{w}$ composed by the bubble best-fit ellipsoid semi-axes, ε_i corresponds to the ith component of the unit vector co-linear with $\vec{w}$:

$$\varepsilon_i = \frac{a_i}{\sqrt{a_k^2}} \tag{7}$$

For each sample, ε_i is the median value over all the bubbles. For spherical bubbles, $\varepsilon_i = 3^{-0.5}$.

For all samples, directional tortuosity, τ_i, was measured using 3dma-rock (Lindquist et al., 1996; Song et al., 2001). 3dma-rock first calculated the sample medial axis network (i.e. the network of paths through the center of bubbles and throats). The two sample faces orthogonal to the selected direction were then taken as entrance and exit faces. For each pair of voxels belonging to each respective face, the shortest path joining them using the medial axis network was calculated. The tortuosity of the voxel pair is the ratio between this shortest path length and the Euclidean distance between the two voxels. For all samples, τ_i is the median tortuosity of all these paths. For isotropic samples, the single tortuosity value, τ, corresponds to the average of the values weighted by the corresponding edge length in the same way as for the permeability values.

2.3. Permeability

Permeability measurements were carried out by numerical simulations of fluid flow within the bubble network. This is now a standard method to measure permeabilities on millimeter-size samples scanned by CT (Wright et al., 2006; Degruyter et al., 2010b; Bai et al., 2010; Polacci et al., 2014). The Lattice Boltzman solver used is Palabos (www.palabos.org), following the procedure described in Degruyter et al. (2010b). Briefly, the CT volumes were considered as a permeable structure where the glass is solid and the bubble space is filled with a fluid of constant density and viscosity. Walls delimiting the porous space are defined as non-slip boundaries. Each simulation was run by applying a pressure difference between two opposite sides orthogonal to the direction of interest, sealing the remaining four sides, and solving for the flow field. The simulations were used to obtain both the viscous, k_1, and inertial, k_2, permeability coefficients according to the Forchheimer equation (Ruth and Ma, 1992; Rust and Cashman, 2004):

$$\frac{dP}{dx_i} = \frac{\mu}{k_1} v_i + \frac{\rho}{k_2} v_i^2 \tag{8}$$

where dP/dx_i is the pressure gradient between two opposite sides of the parallelepipedic sample along direction i, μ is fluid viscosity, ρ is fluid density, and v_i is the average fluid velocity in direction i. Equation (8) is quadratic with respect to v_i, so simulations with different pressure gradients were run in order to find k_1 and k_2. These gradients were such that the Reynolds numbers of the fluid flow through the permeable network were high enough to ensure that inertial effects were present (Table S2 and Supplementary Text S1). The associated Mach numbers were low enough to ensure that the incompressibility assumption was not violated. Six runs were carried out on sample G442 to find the optimal number of simulations. After three simulations, the k_1 value is insensitive to the number of tested pressure gradients, changing by $<0.03\%$ when increasing from 3 to 4 simulations. The value of k_2, however, is more sensitive to the number of tested pressure gradients, changing from 62% to 2% when going from 3 to 4 and then from 4 to 5 simulations, respectively. We chose to interpolate k_1 and k_2 over 4 simulations, which introduces an uncertainty of less than a few percent on both permeability coefficients.

We separately tested the effects of voxel size and CT volume size on permeability (Supplementary Text S1). We used the characteristic number of bubbles across the connected clusters to classify samples as permeable and impermeable. Whether CT volumes are large enough to be representative with respect to permeability was tested following Bai et al. (2010). This analysis suggests that the uncertainty introduced by the finite size of the CT volumes is within a factor 1.5 for k_1 and within a factor 5 for k_2; it is roughly of the same order as the uncertainty given by the three directions of space for nearly equant volumes. It also suggests that the voxel size of the isotropic samples was sufficiently small (edge length is 1–4 µm with bubbles containing an average of 43 voxels across, Table S1) to limit the effect of discretization to $<10\%$ of the permeability values. Because anisotropic samples contain fewer bubbles, the effect of discretization was tested systematically (Table S2). Overall, changing voxel size affects anisotropic permeability values by a factor ranging from 1.4 to 20.

To be able to compare permeability values (k_1 and k_2, respectively) of isotropic samples, regardless of CT volume shape, the three orthogonal directions were measured in turn and a single average value was obtained by weighting each direction by its dimension relative to the three others (i.e. ${}^{avg}k = ({}^{x}k \times x + {}^{y}k \times y + {}^{z}k \times z)/(x+y+z)$, where ${}^{avg}k$ is the average permeability value, x, y, and z are the side lengths of the CT volume, and ${}^{x}k$, ${}^{y}k$, and ${}^{z}k$ are the respective permeabilities). Positive error bars represent the maximum value minus the weighted average and negative error bars represent the weighted average minus the minimum value. No weighting was done for anisotropic samples as permeability in each direction is considered separately. Errors on anisotropic samples represent the effects of grid size. In summary, a total of $4 \times 3 = 12$ simulations were carried out per sample. Simulations were run on the CIMENT computer cluster "gofree" at ISTerre, France, with either 48 or 64 cores, depending on sample size, for a total running time of <3 days per sample.

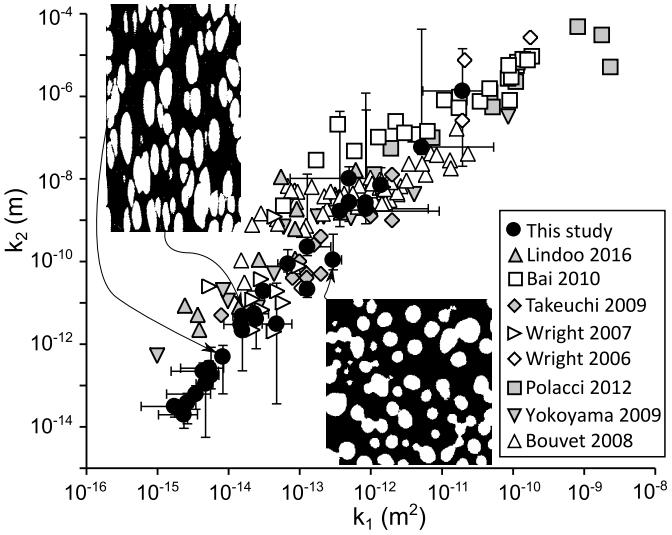

Fig. 1. Viscous permeability (k_1) as a function of inertial (k_2) permeability. Black circles mark our measured values on experimentally decompressed rhyolitic melts, and other symbols represent data from Wright et al. (2006, 2007); Bouvet de Maisonneuve et al. (2009), Yokoyama and Takeuchi (2009), Takeuchi et al. (2009), Bai et al. (2010), Polacci et al. (2012), and Lindoo et al. (2016). Insets show 2D binary images (bubbles are white, glass is black) of an isotropic sample (lower right, G434, sides are 0.81 mm long, permeability indicated with an arrow is measured on a volume of much larger cross-section) and an anisotropic sample (upper left, ABG9b, long side is 0.83 mm, permeabilities along arrow direction indicated).

Because k_1 and k_2 values span as many as 4 orders of magnitude and include 0, fitting by minimizing the ℓ_2-norm (squared Pearson's correlation coefficient, R^2) on the log values of k_1 and k_2 is not possible. We chose instead cubic-root data transformation to calculate the residuals for these two variables and minimized the ℓ_1-norm so that residuals are not dominated by outliers (Horn and Johnson, 1985). The sums of residuals from each fitted equation were normalized by the maximum values of the respective measured variable to ensure that each equation was given comparable weight. Using m and c indices to differentiate between calculated and measured quantities, the residual sums are:

$$R_1 = \frac{\sum |(k_1)_m^{1/3} - (k_1)_c^{1/3}|}{max((k_1)_m^{1/3})}$$
$$R_2 = \frac{\sum |(k_2)_m^{1/3} - (k_2)_c^{1/3}|}{max((k_2)_m^{1/3})} \tag{9}$$
$$R_3 = \frac{\sum |(\phi_c/\phi_t)_m - (\phi_c/\phi_t)_c|}{max((\phi_c/\phi_t))}$$

where ϕ_c and ϕ_t are connected and total porosity, respectively.

3. Results

Fig. 1 shows the calculated viscous and inertial permeability coefficients (Eq. (8)). Viscous permeabilities range from 1.7×10^{-15} to 1.9×10^{-11} m^2, whereas inertial coefficients range from 2.0×10^{-14} to 1.4×10^{-6} m (Table S2). These permeabilities will be referred to as "measured permeabilities" although they are the result

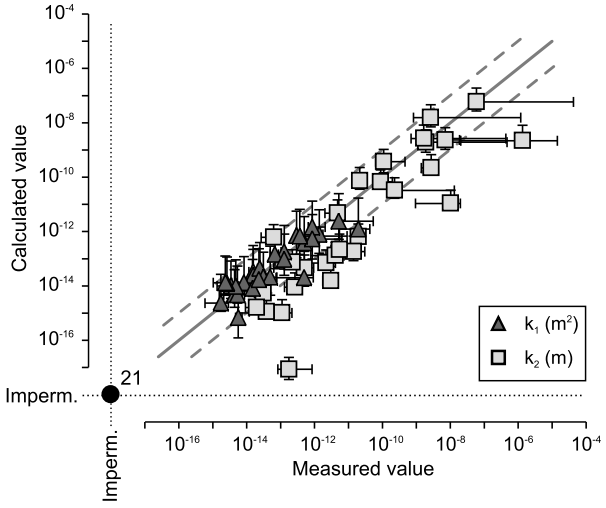

Fig. 2. Measured versus calculated permeabilities (k_1 and k_2). Calculated permeabilities are from Eqs. (10)–(11). The continuous gray line marks the 1:1 ratio and the two dashed gray lines mark the 1:10 and 10:1 ratios, respectively. The two axes labeled "Imperm." represent permeability coefficients of zero and the filled circle with the label "21" represents 21 samples correctly identified as being impermeable.

of computations, so as to differentiate them from values calculated by simplified relationships, which are herein referred to as "calculated permeabilities". The coefficients are correlated and can be fitted by a power law ($k_2 = 4.73 \times 10^{14} k_1^{1.91}$ with $R^2 = 0.97$ on the log values). Such a correlation is consistent with the findings of other studies on natural and experimental products (Fig. 1). This consistency has two consequences. First, it gives confidence in the permeabilities computed from CT volumes, and second it shows that even samples with low (<20) numbers of connected bubbles across one direction yield permeabilities that follow the trend defined by samples that have many connected bubbles. This method is therefore applicable to experimental bubble studies with small sample volumes.

Relationships proposed by Degruyter et al. (2010a) link both permeability coefficients to physical parameters of the permeable network:

$$k_1 = \frac{\phi_c^n d_t^2}{16 \chi \tau^2} \tag{10}$$

$$k_2 = \frac{\phi_c^{4n} d_t^2}{2 f_0 \tau^3} \tag{11}$$

where d_t is the characteristic diameter of the bubble connections (throats), χ is the channel circularity here measured on the bubbles, τ is the tortuosity of the connected bubble network, and f_0 is an inertial friction coefficient. For anisotropic samples, ϕ_c, τ, and χ should henceforth be replaced by ϕ_{c-i}, τ_i and χ_i, where $i = x$, y, or z is the direction considered. Compared to Degruyter et al. (2010a), we changed 1 into n in the exponent of ϕ_c in Eq. (10) and 2 into $4n$ in the exponent of ϕ_c in Eq. (11) because, although k_1 and k_2 are related to first order by a power law, the ratio k_2/k_1 has a second-order dependence on ϕ_c^4 (Fig. S3). Our measurements of the bubble network provide values for every parameters of Eqs. (10)–(11), except n and f_0. A two-parameter regression minimizing $R_1 + R_2$ (Eq. (9)) yields best fits values of $n = 2.49$ and $f_0 = 1.21$ with $R_1 = 1.69$ and $R_2 = 1.47$ (Fig. 2). The fit is better for k_1 than for k_2, with 26 out of 28 samples having calculated values within one log unit of the measured k_1 value and only 13 out of 28 calculated k_2 being within one log unit of the measured k_2. The k_2 value of sample G437 is an outlier for which no explanation has been found.

The core of the percolation concept is that not all gas bubbles belong to the connected network. By depending on the connected porosity, Eqs. (10)–(11) assume that the percolation state of the sample is known. Were it not the case, ϕ_c would be unknown and no impermeable samples would be correctly identified as such. This implies that these equations correctly identify the permeability state of only 57% of the samples if percolation information is missing. Equations (10)–(11) also rely on network parameters that are not traditionally available in most studies and in conduit flow models, such as bubble throat diameters or tortuosity. We relax these assumptions by linking the variables ϕ_c, d_t, and τ to a combination of ϕ_t, d_a, and σ_a.

Polacci et al. (2014) suggested that throat diameters can be related to average bubble diameters. In each of our samples, the distribution of the ratios of throat dimension over the diameter of the neighboring bubble is wide and mostly unimodal (Fig. S4), which drove us to characterize each sample by a median throat/bubble ratio. Bringing all samples together, these ratios have values clustering around 0.4 (Fig. 3A): $d_t = 0.4 \times d_a$.

Tortuosity can be related to connected porosity by Archie's law (Wright et al., 2009; Degruyter et al., 2010a):

$$\tau^2 = \phi_c^{1-m} \tag{12}$$

where m is a constant named the formation factor ($m \geq 1$). Tortuosity depends on bubble shape (Degruyter et al., 2010a). Bubbles elongated parallel to the main gas flow direction decrease the tortuosity in that direction. Conversely, bubbles elongated perpendicular to gas flow increase tortuosity. Here we add an empirical pre-factor to Eq. (12) to take into account bubble anisotropy, using i indices for clarity:

$$\tau_i^2 = \frac{c_\tau \chi_i}{2\sqrt{3}\varepsilon_i} \phi_c^{1-m} \tag{13}$$

where c_τ is an empirical constant, ε_i is a measure of bubble elongation in direction i, χ_i is the cross-section shape factor orthogonal to i, and the factor $2\sqrt{3}$ is such that the pre-exponential factor is equal to c_τ for isotropic samples. We find that the best-fit factor, c_τ, and exponent, m, are 4 and 1, respectively (Fig. S5). Dropping the i indices, tortuosity in a given direction is thus equal to:

$$\tau^2 = (2\chi)/(\sqrt{3}\varepsilon) \tag{14}$$

with $R^2 = 0.64$. Equation (14) no longer depends on ϕ_c. This fit thus ensures a better representation of the effect of bubble elongation on τ at the expense of capturing the influence of ϕ_c on τ.

The lack of a single porosity threshold for percolation found by previous studies suggests that the threshold does not depend solely on porosity. The observation that bubble size distributions are more disperse in permeable samples than in impermeable samples (Burgisser and Gardner, 2004) led us to explore the idea that inter-bubble melt thickness may be a controlling parameter for bubble connectivity. We found that the measured bubble separation distance, z_m, weighted by the normalized degree of polydispersity of the bubble size distribution, σ_a/d_a, (i.e. the quantity $z_m(\sigma_a/d_a)^{c_z}$ with c_z a constant) is an excellent discriminant between permeable and impermeable samples (Fig. 3B). All samples but two can be correctly assigned to a permeability state, based on a critical value of $z_m(\sigma_a/d_a)^{-1}$.

One difficulty is that the inter-bubble distance involved in the discriminatory quantity $z_m(\sigma_a/d_a)^{-1}$ is not traditionally measured in magmatic products, because bubble spacing is generally deduced from bubble size and total porosity in different ways (e.g., Lensky et al., 2004; Castro et al., 2012; Mancini et al., 2016). Our data allow us to re-evaluate such relationships (Fig. 3C), and we

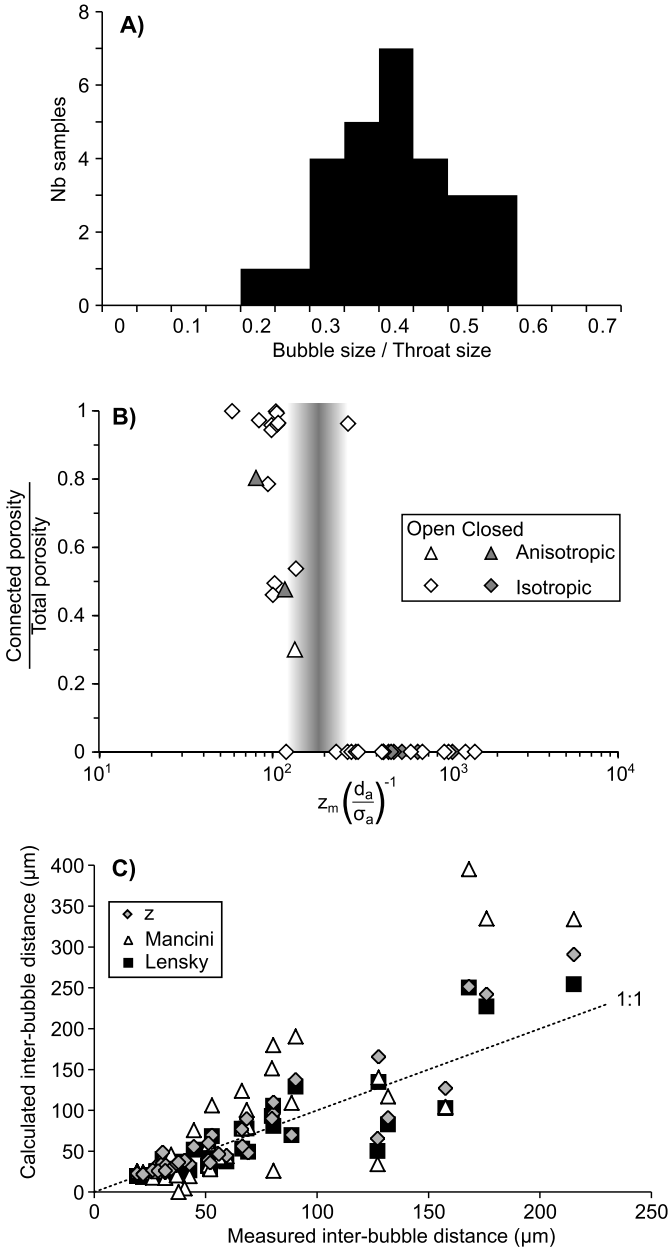

Fig. 3. Relationships between parameters of the bubble networks. A) Histogram of the median ratio d_a/d_t. B) Sorting criteria in μm (inter-bubble distance, z_m, divided by σ_a/d_a) as a function of connectivity (ϕ_c/ϕ_t). Samples are sorted in decompression style ("open" vs. "closed" system) and bubble shapes ("isotropic" vs. "anisotropic"). The shaded vertical area suggests a limit between permeable and impermeable samples. C) Measured inter-bubble distance as a function of calculated inter-bubble distance. Symbols mark three calculation methods: "z" is that of Eq. (15), "Mancini" is that of Mancini et al. (2016) (their z_1 with $o = 6$ and $\alpha_p = 0.63$), and "Lensky" is that of Lensky et al. (2004).

found that the following expression is a good compromise between algebraic simplicity and accuracy:

$$z = 1.5 d_a (\phi_t^{-1/3} - 1) \tag{15}$$

which fits our data with $R^2 = 0.8$. A percolation threshold can thus be defined using $Z = z(\sigma_a/d_a)^{c_z}$, instead of $z_m(\sigma_a/d_a)^{-1}$. Moreover, the behavior of ϕ_c/ϕ_t can be described by a logistic function that tends to 1 for small values of Z and to 0 for large Z values:

$$\frac{\phi_c}{\phi_t} = \frac{1}{1 + \exp(-c_\phi (Z - c_p))} \tag{16}$$

where c_ϕ and c_p are fit parameters.

Summarizing these simplifications, we can write a viscous permeability relationship that depends only on the average and standard deviation of the bubble size distribution, the average bubble aspect ratio, and the total porosity:

$$k_1 = \frac{\phi_c^n d_a^2 \sqrt{3}\varepsilon}{200\chi^2} \tag{17}$$

where tortuosity is derived using Eq. (14), and n is a constant to be determined. Similarly, the inertial permeability can be expressed as:

$$k_2 = \frac{\phi_c^{4n} d_a}{5 f_0} \left(\frac{\sqrt{3}\varepsilon}{2\chi} \right)^{3/2} \tag{18}$$

The connected porosity is obtained by using Eq. (16) with the inter-bubble distance z from Eq. (15):

$$\phi_c = \frac{\phi_t}{1 + \exp(-c_\phi (1.5 d_a (\phi_t^{-1/3} - 1) - c_p))} \tag{19}$$

There are thus five parameters (c_z, c_ϕ, c_p, n, and f_0) that need to be determined, whereas five measured geometric quantities (ϕ_t, d_a, σ_a, χ, and ε) can be entered into Eqs. (17)–(19) to calculate three quantities (ϕ_c/ϕ_t, k_1, and k_2) that can be compared with their measured counterparts. Five parameters to be regressed simultaneously are too many degrees of freedom for the two-parameter linear regression used to fit Eqs. (10)–(11) in Fig. 2. We instead used a grid search technique to minimize the ℓ_1-norm (Eq. (9)). The sum $R_1 + R_2 + R_3$ was minimized by nested grid search within the bounds $-1 < c_z < 0$, $-10^6 < c_\phi < 0$, $10^{-5} < c_p < 10^{-4}$, $2 < n < 4$, and $10^{-2} < f_0 < 10^2$. To keep grid points within a computationally manageable number, the grid search was conducted with a precision on each parameter that yielded three significant digits, which gave $c_z = -0.128$, $c_\phi = -0.342 \times 10^6$, $c_p = 33.2 \times 10^{-6}$, $n = 2.73$, and $f_0 = 0.790$ with $R_1 = 2.59$, $R_2 = 1.73$, and $R_3 = 5.65$.

Fig. 4A shows ϕ_c/ϕ_t as a function of Z and the fit of Eq. (19) with the above values of c_z, c_ϕ, and c_p (the goodness of fit of ϕ_c is shown on Fig. S6). By definition, $\phi_c/\phi_t = 0.5$ when $Z = c_p$, and the absence of percolation corresponds to ϕ_c/ϕ_t approaching 0. A percolation threshold can thus be defined as a critical value of either ϕ_c/ϕ_t or Z. For simplicity, we chose to define the percolation threshold as $Z_p = c_p + c_d$, where c_d is an additional parameter to be determined. This implies that the threshold value of ϕ_c/ϕ_t is $(1 + \exp(-c_\varphi c_d))^{-1}$. We varied c_d to maximize the number of successfully attributed permeability states and found that c_d values from 3×10^{-6} to 8×10^{-6} ensure that the permeability state of all samples but two are correctly identified (Fig. 4A). Using Eq. (15) in conjunction with the discriminant $Z_p = z(\sigma_a/d_a)^{c_z}$ we can define the percolation porosity threshold, ϕ_p, as:

$$\phi_p = \left[1 + \frac{c_p + c_d}{1.5 d_a} \left(\frac{\sigma_a}{d_a} \right)^{0.128} \right]^{-3} \tag{20}$$

where $c_p + c_d = 39.2 \pm 3 \times 10^{-6}$ m marks the percolation threshold for our samples that correctly identifies the permeability state of 96% of the samples.

Fig. 4B compares calculated and measured permeabilities for the fitted relationships (Eqs. (17)–(19)). Overall, Fig. 4B suggests that most viscous permeability coefficients are predicted within one order of magnitude (88% of the cases), but that only 54% of the inertial permeability coefficients are predicted within one order of magnitude (88% within a factor 100). The same k_2 outlying value as in Fig. 2 is present because the calculated values

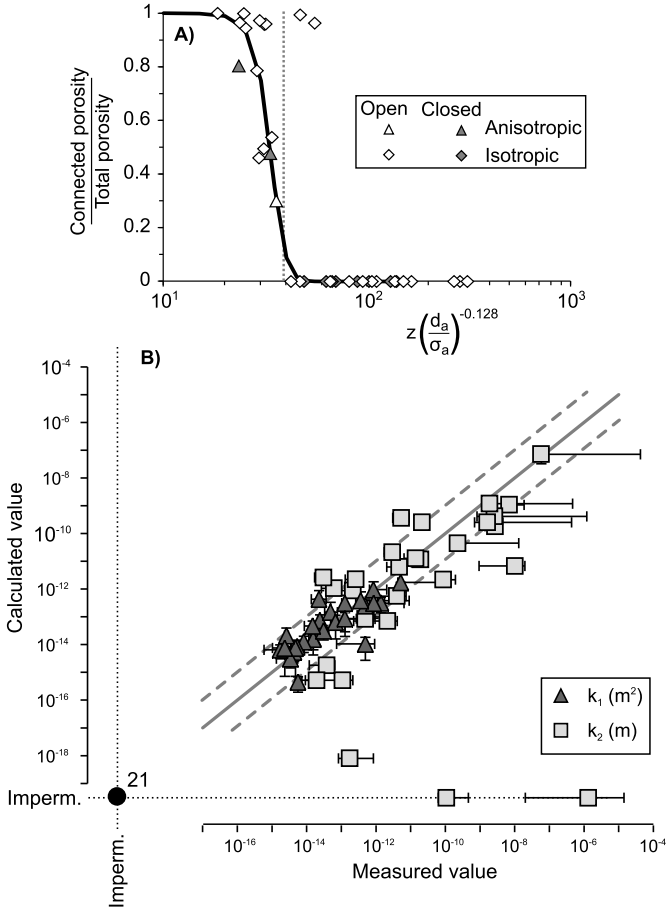

Fig. 4. Results of the fitting procedure. A) Sorting criteria in μm (calculated inter-bubble distance, z, times a power law of σ_a/d_a) as a function of connectivity (ϕ_c/ϕ_t). Samples are sorted in decompression style ("open" vs. "closed" system) and bubble shapes ("isotropic" vs. "anisotropic"). The bold curve is Eq. (19). The vertical dashed line marks the critical value that defines percolation and distinguishes all impermeable samples from permeable samples except two. B) Measured versus calculated permeabilities (k_1 and k_2). The continuous gray line marks the 1:1 ratio and the two dashed gray lines mark the 1:10 and 10:1 ratios, respectively. The two axes labeled "Imperm." represent permeability coefficients of zero and the filled circle with the label "21" represents 21 samples correctly identified as being impermeable. Two samples incorrectly identified as being impermeable are on the horizontal impermeable axis.

of ϕ_c, d_t, and τ for that sample (G437) are close to the corresponding measurements. For isotropic samples, permeabilities can simply be expressed as $k_1 = \phi_c^{2.73} d_a^2/800$ and $k_2 = \phi_c^{10.92} d_a/(8 f_0)$. For strongly anisotropic samples, k_1 could be more than one order of magnitude below the isotropic equivalent value (at most by a factor 20 if χ and ε have the highest measured values of 6 and 0.25, respectively).

4. Discussion

4.1. Comparison of permeability relationships

We evaluate our results against two widely used relationships that aim at quantifying permeability from geometrical measurements of the porous network. The first is a Kozeny–Carman relationship between viscous permeability and porosity (e.g., Eichelberger et al., 1986; Klug and Cashman, 1996; Rust and Cashman, 2011):

$$k_1 = a_{KC} \phi_c^{b_{KC}} \tag{21}$$

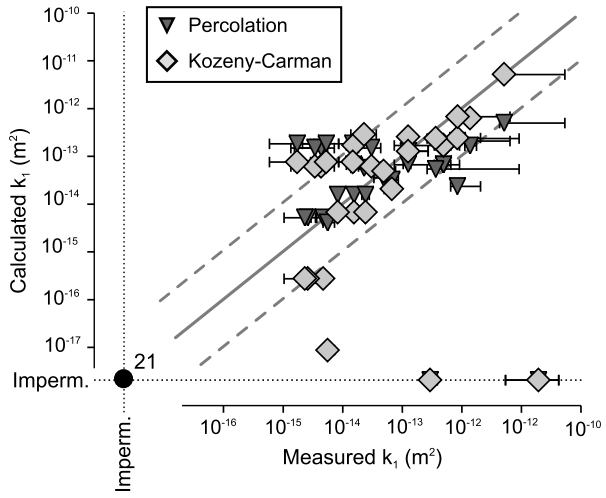

Fig. 5. Measured versus calculated permeability (k_1) from Eq. (21) ("Kozeny–Carman") and Eq. (22) ("Percolation"). Errors are only reported for measured quantities. The continuous gray line marks the 1:1 ratio and the two dashed gray lines mark the 1:10 and 10:1 ratios, respectively. The two axes labeled "Imperm." represent permeability coefficients of zero and the filled circle with the label "21" represents 21 samples correctly identified as being impermeable. Two samples incorrectly identified as being impermeable are the horizontal impermeable axis.

where a_{KC} and b_{KC} are fitted constants. Using Eq. (19) to express ϕ_c, a two-parameter best fit yields $a_{KC} = 8.27 \times 10^{-11}$ m^2 and $b_{KC} = 6.02$ with $R_1 = 2.75$ (Fig. 5).

The second relationship highlights that total porosity and connected porosities are distinct by explicitly depending on total porosity, ϕ_t, and the percolation threshold, ϕ_p (e.g., Feng et al., 1987; Sahini and Sahimi, 1994; Saar and Manga, 1999; Mueller et al., 2005):

$$k_1 = a_M (\phi_t - \phi_p)^{b_M} \tag{22}$$

where a_M and b_M are fitted constants. Setting $\phi_p = 15$ vol.% ensures that all permeable samples are correctly identified as such, but only 2 out of the 21 impermeable samples are correctly identified. Conversely, setting $\phi_p = 60$ vol.%, only 2 out of 28 permeable samples, yet all impermeable samples, are correctly identified. This illustrates that no single value of ϕ_p explains the variation of our data (Mueller et al., 2005). Using Eq. (20) to express ϕ_p, all samples but two are correctly identified and a two-parameter best fit yields $a_M = 1.85 \times 10^{-11}$ m^2 and $b_M = 2.49$ with $R_1 = 3.64$ (Fig. 5).

In summary, the original Degruyter Eq. (10) yields the best fits for the viscous permeability, followed by our simplified Eq. (17), the Kozeny–Carman relationship, and the percolation relationship (R_1 values of 1.69, 2.59, 2.75, and 3.64, respectively). Much of the predictive capability is lost when network parameters such as ϕ_c or τ are not available. When these parameters are missing, regression results give a slight advantage to our relationship compared to that of Kozeny–Carman.

4.2. Testing the percolation threshold against other data sets

Our percolation threshold can be evaluated against published data sets by comparing the calculated threshold to measured values of ϕ_c/ϕ_t. We selected five studies on natural and experimental magmas with various crystal contents and bubble elongations that provide independent estimates of ϕ_c, ϕ_t, d_a, and σ_a (Burgisser and Gardner, 2004; Bouvet de Maisonneuve et al., 2009; Takeuchi et al., 2009; Okumura et al., 2012; Lindoo et al., 2016). Values of d_a and σ_a were recalculated from the original size distributions when necessary. The percolation threshold depends on an empirical constant, c_p, that our data constrain to be between 3×10^{-6}

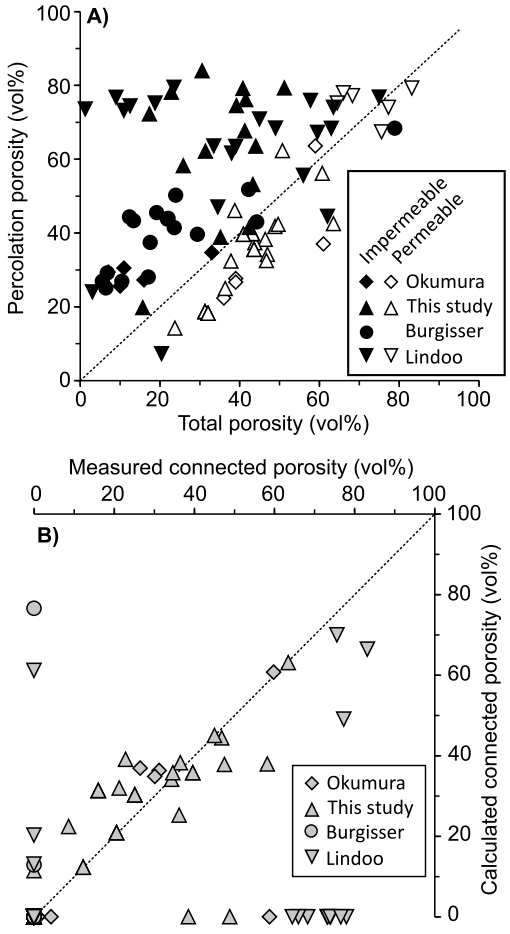

Fig. 6. Applications of the percolation relationship. Data are from Okumura et al. (2012), Burgisser and Gardner (2004), Lindoo et al. (2016), and this study. A) Total porosity (ϕ_t) as a function of percolation porosity (ϕ_p). The dotted line indicates the 1:1 ratio that separates permeable (upper left) from impermeable (lower left) fields. Open symbols are permeable samples and closed symbols are impermeable samples. B) Measured vs. calculated connected porosity (ϕ_c).

and 8×10^{-6} m. This range of c_p values correctly discriminates >87% of all the data points (88% when $c_d = 4 \times 10^{-6}$, Fig. 6A) and Eq. (19) recovers the ϕ_c values of the permeable samples with $R^2 = 0.77$ (Fig. 6B). A global permeability relationship can thus be defined by setting that ϕ_c is given by Eq. (19) when $\phi_t \geq \phi_p$ (or $z \times (\sigma_a/d_a)^{-0.128} \leq 3.72 \times 10^{-5}$) and zero when $\phi_t < \phi_p$. The fact that a success rate of 100% cannot be achieved is partly due to the extreme simplicity of Eqs. (19)–(20), which seek to characterize with a single scalar the percolation state of a complex bubble network where bubbles have heterogeneous shapes and spatial distributions.

Our simplified relationships are more accurate for k_1 than for k_2. Unfortunately, we found no published data set providing independent measures of all the parameters used in Eqs. (17)–(18) to conduct a rigorous evaluation of our relationships. We note, however, that no technical obstacle prevents collecting the relevant data using CT imaging (e.g., Castro et al., 2012), traditional image analysis (e.g., Gardner et al., 1999), or stereology methods (e.g., Martel and Iacono-Marziano, 2015). Because k_2 involves an additional independent parameter, f_0, the lower accuracy on k_2 suggests that considering f_0 as a constant is an oversimplification. This is in agreement with the findings of Degruyter et al. (2010a) and Bouvet de Maisonneuve et al. (2009), which not only indicate that 0.8 is in the low range of inferred f_0 values but also suggest that f_0 should be linked to measurable parameters of the permeable network.

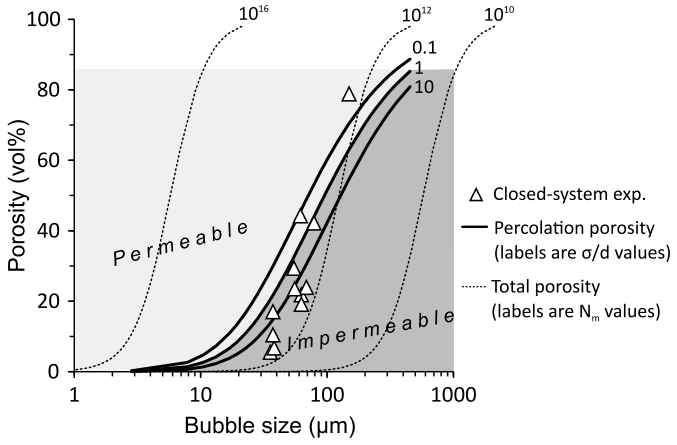

Fig. 7. Total (ϕ_t) and percolation (ϕ_p) porosities as a function of bubble size. Triangle are experimental samples. Dotted curves are total porosities for three bubble number densities (labels 10^{10}, 10^{12}, and 10^{16}). Thick solid curves are percolation porosities for three σ_a/d_a values (labels 0.1, 1, and 10). The light gray field is above the percolation threshold corresponding to $\sigma_a/d_a = 1$ ("permeable") and the dark gray field is below that threshold ("impermeable").

In summary, the simplified relationships we propose give a close representation of the percolation threshold in both experimental and natural products at the expense of a moderate precision on the permeability values compared to laws depending on bubble network parameters. Our laws are related to the connection between gas bubbles in magmas, which means that they are not valid when brittle fracturing occurs (Farquharson et al., 2016; Heap and Kennedy, 2016; Kushnir et al., 2016).

4.3. Implications for magma degassing and eruptions

Having a relationship that estimates percolation has implications for determining at which point gas escapes from magma during ascent. Total porosity and bubble size can be related to the bubble number density per amount of melt, N_m, if the bubble size distribution is monodisperse. The percolation porosity, on the other hand, depends on bubble size and σ_a/d_a. Fig. 7 shows the evolution of ϕ_p and ϕ_t as a function of bubble size for different values of N_m and σ_a/d_a. One trend of percolation porosity is shown for $N_m = 10^{12}$ m^{-3} and three values of σ_a/d_a (0.1, 1, and 10), which approach the conditions of a subset of our data that underwent closed-system decompression and remained impermeable until very large (~80 vol%) porosities. Fig. 7 illustrates how percolation is expected to vary in natural cases. The natural range of N_m is 10^{10}–10^{16} m^{-3} (Rust and Cashman, 2011). The lower bound of σ_a/d_a is 0.1 (our data; Gardner et al., 1999), and the upper bound can be set to 10 by considering that natural pumice often have log normal to exponential distributions (e.g., Polacci et al., 2014). The natural range of parameters can thus be represented by the three ϕ_p curves of Fig. 7 and two additional ϕ_t curves for $N_m = 10^{10}$ and 10^{16} m^{-3}. Fig. 7 shows that high bubble number densities favor percolation at low porosity and early gas loss during ascent whereas low number densities hinder percolation and yield late gas leakage during ascent. The transition predicted by Eq. (20) between impermeable behavior at depth and permeable behavior more shallowly thus spans the full range of percolation porosities inferred in previous studies (Rust and Cashman, 2011; Lindoo et al., 2016).

Fig. 8A represents k_1 versus ϕ_t for our permeability formulation alongside four relationships that are representative of those currently used in conduit flow modeling (Klug and Cashman, 1996; Mueller et al., 2005; Kozono and Koyaguchi, 2009). Increasing N_m in our relationship causes both the percolation threshold and permeability to decrease, whereas, at constant N_m, decreasing σ_a/d_a

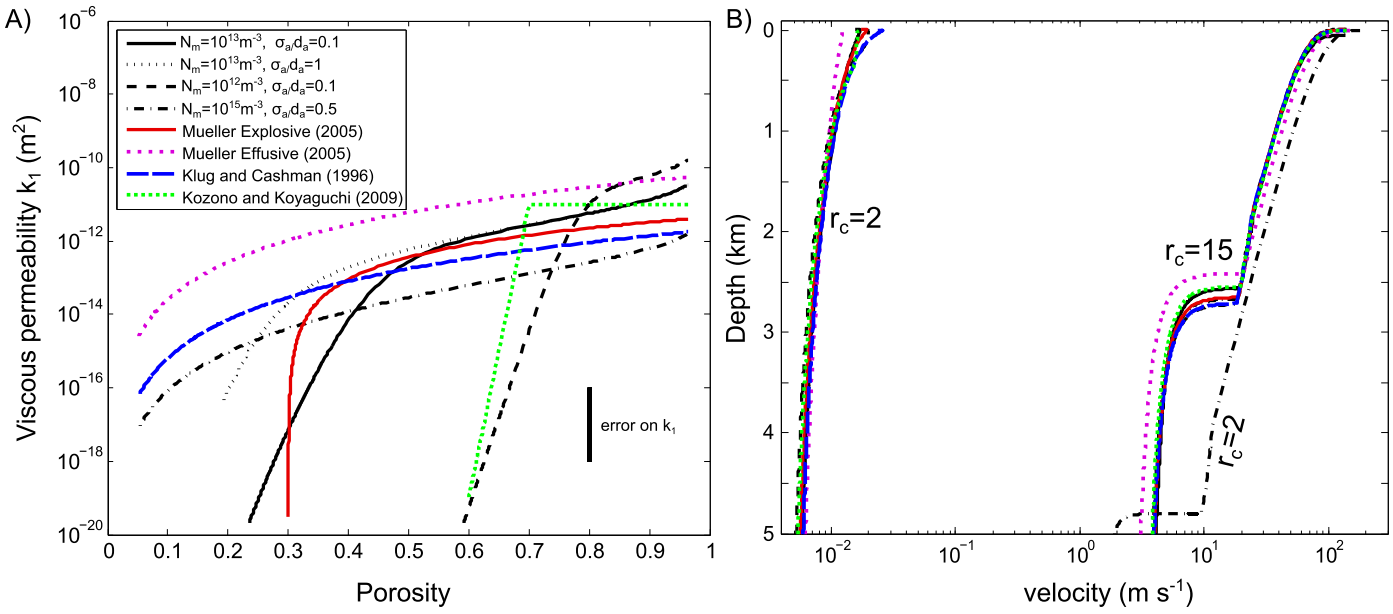

Fig. 8. Influence of various permeability relationships on conduit flow modeling. A) Permeability versus total porosity. B) Model outputs (ascent velocity vs. depth) from the 1D conduit flow model with a conduit radius of 2 and 15 m (labels r_c) and a conduit length of 5 km, a lithostatic pressure at the conduit base with 5 wt.% total water in the magma, and a magma temperature of 950 °C with 45 vol.% crystals. Only liquid velocities are shown. Gas and liquid have velocities that very similar for all runs except effusive runs at depth <1 km, where gas velocities sharply increase to 1–10 m/s. Permeability relationships are from Mueller et al. (2005) for effusive samples ($a_M = 6.3 \times 10^{-11}$ m^2, $b_M = 3.4$) and explosive samples ($a_M = 9 \times 10^{-12}$ m^2, $b_M = 2$), Klug and Cashman (1996, $a_{KC} = 2 \times 10^{-12}$ m^2, $b_{KC} = 3.5$), Kozono and Koyaguchi (2009, $k_1 = 10^{-11}$ m^2 if $\phi_t > 0.7$ with a smooth increase to that constant value when $0.6 < \phi_t < 0.7$), and this study (labels indicate respective values of N_m and σ_a/d_a).

increases the percolation threshold. Setting, for instance, N_m to 10^{15} m^{-3} and σ_a/d_a to 0.5 results in a permeability–porosity relationship that is close to that of Eq. (21). Fig. 8A shows that varying both N_m and σ_a/d_a results in permeability–porosity relationships that cover the same range as those currently used in conduit flow models, except at low porosities ($\phi_t < 0.2$).

Because our relationship depends on parameters widely used in conduit flow modeling, it can be integrated to such numerical models. We implemented it in a 1D two-phase (gas and liquid) conduit flow model tailored to the eruptive conditions prevailing at Merapi volcano in 2010 (e.g., Costa et al., 2013; Erdmann et al., 2016). We used the Kozono and Koyaguchi (2009) model, as modified by Degruyter et al. (2012), to include inertial permeability and the effect of dissolved water on melt viscosity. The effect of crystals on magma viscosity was calculated using Krieger and Dougherty (1959) with a maximum packing 0.65 and an Einstein coefficient of 2.5. Equations (17)–(20) require the specification of d_a, ϕ_t, ε, χ, and σ_a/d_a. Bubble diameter and ϕ_t were calculated from N_m and the melt water content. To be consistent with Fig. 8A, N_m was varied from 10^{12} to 10^{15} m^{-3} and σ_a/d_a was varied from 0.1 to 1. Parameters ε and χ can be estimated using relationships between flow conditions and bubble elongation and orientation (e.g. Rust et al., 2003). In 1D modeling, however, assigning a single preferential orientation at each depth is complex, because the amounts of simple and pure shear have to be averaged over the conduit cross-section. Using the constant values of $\varepsilon = 3^{-0.5}$ and $\chi = 2$ is acceptable because ε and χ have only a second-order influence on permeability. We assume that gas flow was laminar for the four published permeability relationships because they do not include k_2.

Fig. 8B presents model results as liquid (melt + crystals) velocities versus depth. Although we used permeability relationships that cover a wide range of percolation thresholds and permeabilities, model outputs are similar for the eruptive conditions we considered. When the conduit radius is set to 15 m, all runs are in the explosive regime with differences in velocity profiles within 0.15 log units of each other. They have similar fragmentation depths of 2580 ± 170 m and mass fluxes of 5.21–6.91 × 10^6 kg/s. When conduit radius is set to 2 m, all runs are effusive with mass fluxes ranging from 157 to 185 kg/s, except for the run corresponding to $N_m = 10^{15}$ m^{-3} and $\sigma_a/d_a = 0.5$, which is explosive with a mass flux of 5.67 × 10^4 kg/s and a fragmentation depth of 4800 m. With only one run over sixteen having a distinct behavior, the influence of permeability and percolation is thus small under such conditions. The model we use assumes that gas separates from the magma by flowing only in the vertical direction, although a significant part of gas losses during ascent could occur through leakage at the conduit walls (Jaupart and Allègre, 1991; Collombet, 2009). Although such a characterization is beyond the scope of this work, we intuit that our percolation and permeability relationships have more influence in other types of conduit flow models.

In the anisotropic samples we use to establish the percolation threshold, the deformation is due to sample decompression that induced pure shear (Burgisser and Gardner, 2004). The amplitude of this deformation remains relatively low (maximum aspect ratio of 6). Several studies have shown that simple shear can significantly decrease the percolation threshold when it reaches high amplitudes (e.g., Caricchi et al., 2011; Okumura et al., 2009, 2013). Unlike pure shear, simple shear involves bubble rotation that enhances bubble interaction and coalescence. As simple shear is expected to occur in volcanic conduits during magma ascent, it may affect percolation and permeability development in a way that is not captured by our data set.

5. Conclusions

We present results on permeability and bubble network determinations of experimental samples that were decompressed at 6 × 10^{-3}–10 MPa/s from 150 MPa down to 60–15 MPa. Samples were crystal-free rhyolitic melts bearing 10–64 vol% of H_2O bubbles with aspect ratios of 2–6, sizes of 4–350 μm, and number densities of 5 × 10^{10}–5 × 10^{13} m^{-3}. Samples were analyzed by X-ray microtomography to image the bubble networks in 3D. From measurements of the 3D images and geometrical considerations,

we develop a percolation threshold for magmas that depends on the bubble network characteristics. This relationship, which is calibrated on our sample set, recovers the behavior of a wide range of experimental and natural volcanic samples, from basaltic andesite to rhyolite, and from crystal-free to crystal-rich. It separates permeable samples from impermeable ones with a success rate of 88%.

We propose simplified permeability relationships based on the percolation threshold that rely on parameters widely used in magma flow numerical modeling. They are calibrated on our sample set and they are valid within one order of magnitude for the viscous permeability coefficient and within two orders of magnitude for the inertial permeability coefficient. They recover the ranges of values previously covered by isolated relationships, reassembling them within a single framework. The implications of such a unification on eruptive dynamics is tested by using a 1D, two-phase conduit flow model constrained by conditions prevailing during the 2010 eruption of Merapi volcano. Results suggest that varying the percolation threshold has little influence on vertical gas loss and ascent dynamics.

Acknowledgements

We appreciated the thorough and helpful reviews by W. Degruyter, the editor, and an anonymous reviewer. This project was partially funded by the European Research Council (grant 202844 under the European FP7), by the ANR DoMerapi (ANR-12-BS06-0012), and by a grant from Labex OSUG@2020 (Investissements d'avenir – ANR10 LABX56). JMC is supported by the VAMOS research centre, University of Mainz, Germany.

Appendix A. Supplementary material

Supplementary material related to this article can be found online at http://dx.doi.org/10.1016/j.epsl.2017.04.023.

References

Bai, L., Baker, D.R., Hill, R.J., 2010. Permeability of vesicular Stromboli basaltic glass: lattice Boltzmann simulations and laboratory measurements. J. Geophys. Res. 115. http://dx.doi.org/10.1029/2009JB007047.

Blower, J.D., 2001. Factors controlling permeability–porosity relationships in magma. Bull. Volcanol. 63, 497–504.

Bolte, S., Cordelières, F.P., 2006. A guided tour into subcellular colocalization analysis in light microscopy. J. Microsc. 224, 213–232. http://dx.doi.org/10.1111/j.1365-2818.2006.01706.x.

Bouvet de Maisonneuve, C., Bachmann, O., Burgisser, A., 2009. Characterization of juvenile pyroclasts from the Kos Plateau Tuff (Aegean Arc): insights into the eruptive dynamics of a large rhyolitic eruption. Bull. Volcanol. 71, 643–658. http://dx.doi.org/10.1007/s00445-008-0250-x.

Burgisser, A., Gardner, J.E., 2004. Experimental constraints on degassing and permeability in volcanic conduit flow. Bull. Volcanol. 67, 42–56. http://dx.doi.org/10.1007/s00445-004-0359-5.

Caricchi, L., Pommier, A., Pistone, M., Castro, J., Burgisser, A., Perugini, D., 2011. Strain-induced magma degassing: insights from simple-shear experiments on bubble bearing melts. Bull. Volcanol. 73, 1245–1257. http://dx.doi.org/10.1007/s00445-011-0471-2.

Castro, J.M., Burgisser, A., Schipper, C.I., Mancini, S., 2012. Mechanisms of bubble coalescence in silicic magmas. Bull. Volcanol. 74, 2339–2352. http://dx.doi.org/10.1007/s00445-012-0666-1.

Collombet, M., 2009. Two-dimensional gas loss for silicic magma fows: toward more realistic numerical models. Geophys. J. Int. 177, 309–318.

Costa, F., Andreastuti, S., Bouvet de Maisonneuve, C., Pallister, J.S., 2013. Petrological insights into the storage conditions, and magmatic processes that yielded the centennial 2010 Merapi explosive eruption. J. Volcanol. Geotherm. Res. 261, 209–235. http://dx.doi.org/10.1016/j.jvolgeores.2012.12.025.

Degruyter, W., Bachmann, O., Burgisser, A., 2010a. Controls on magma permeability in the volcanic conduit during the climactic phase of the Kos Plateau Tuff eruption (Aegean Arc). Bull. Volcanol. 72, 63–74. http://dx.doi.org/10.1007/s00445-009-0302-x.

Degruyter, W., Burgisser, A., Bachmann, O., Malaspinas, O., 2010b. Synchrotron X-ray microtomography and lattice Boltzmann simulations of gas flow through volcanic pumices. Geosphere 6, 470–481.

Degruyter, W., Bachmann, O., Burgisser, A., Manga, M., 2012. The effects of outgassing on the transition between effusive and explosive silicic eruptions. Earth Planet. Sci. Lett. 349–350, 161–170. http://dx.doi.org/10.1016/j.epsl.2012.06.056.

Doube, M., Kłosowski, M.M., Arganda-Carreras, I., Cordelières, F.P., Dougherty, R.P., Jackson, J.S., Schmid, B., Hutchinson, J.R., Shefelbine, S.J., 2010. BoneJ: free and extensible bone image analysis in ImageJ. Bone 47, 1076–1079. http://dx.doi.org/10.1016/j.bone.2010.08.023.

Eichelberger, J.C., Carrigan, C.R., Westrich, H.R., Price, R.H., 1986. Non-explosive silicic volcanism. Nature 323, 598–602.

Erdmann, S., Martel, C., Pichavant, M., Bourdier, J.-L., Champallier, R., Komorowski, J.-C., Cholik, N., 2016. Constraints from phase equilibrium experiments on pre-eruptive storage conditions in mixed magma systems: a case study on crystal-rich basaltic andesites from Mount Merapi, Indonesia. J. Petrol. 57, 535–560. http://dx.doi.org/10.1093/petrology/egw019.

Farquharson, J.I., Heap, M.J., Lavallée, Y., Varley, N.R., Baud, P., 2016. Evidence for the development of permeability anisotropy in lava domes and volcanic conduits. J. Volcanol. Geotherm. Res. 323, 163–185. http://dx.doi.org/10.1016/j.jvolgeores.2016.05.007.

Feng, S., Halperin, H.I., Sen, P.N., 1987. Transport properties of continuum systems near the percolation threshold. Phys. Rev. B 35, 197–214.

Gardner, J.E., 2007. Bubble coalescence in rhyolitic melts during decompression from high pressure. J. Volcanol. Geotherm. Res. 166, 161–176.

Gardner, J.E., Hilton, M., Carroll, M.R., 1999. Experimental constraints on degassing of magma: isothermal bubble growth during continuous decompression from high pressure. Earth Planet. Sci. Lett. 168, 201–218.

Gonnermann, H.M., Manga, M., 2007. The fluid mechanics inside a volcano. Annu. Rev. Fluid Mech. 39, 321–356.

Heap, M.J., Kennedy, B.M., 2016. Exploring the scale-dependent permeability of fractured andesite. Earth Planet. Sci. Lett. 447, 139–150. http://dx.doi.org/10.1016/j.epsl.2016.05.004.

Horn, R.A., Johnson, C.R., 1985. Norms for vectors and matrices. In: Matrix Analysis. Cambridge University Press.

Jaupart, C., Allègre, C., 1991. Gas content, eruption rate and instabilities of eruption regime in silicic volcanoes. Earth Planet. Sci. Lett. 102, 413–429.

Ketcham, R.A., 2005. Computational methods for quantitative analysis of three-dimensional features in geological specimens. Geosphere 1, 32–41.

Klug, C., Cashman, K.V., 1996. Permeability development in vesiculating magmas: implications for fragmentation. Bull. Volcanol. 58, 87–100.

Kozono, T., Koyaguchi, T., 2009. Effects of relative motion between gas and liquid on 1-dimensional steady flow in silicic volcanic conduits: 1. An analytical method. J. Volcanol. Geotherm. Res. 180, 21–36.

Krieger, I.M., Dougherty, T.J., 1959. A mechanism for non-Newtonian flow in suspensions of rigid spheres. Trans. Soc. Rheol. III, 137–152.

Kushnir, A.R.L., Martel, C., Bourdier, J.-L., Heap, M.J., Reuschle, T., Erdmann, S., Komorowski, J.-C., Cholik, N., 2016. Probing permeability and microtexture: unravelling the role of a low-permeability dome on the explosivity of Merapi (Indonesia). J. Volcanol. Geotherm. Res. 316, 56–71.

Lensky, N.G., Navon, O., Lyakhovsky, V., 2004. Bubble growth during decompression of magma: experimental and theoretical investigation. J. Volcanol. Geotherm. Res. 129, 7–22.

Lindoo, A., Larsen, J.F., Cashman, K.V., Dunn, A.L., Neill, O.K., 2016. An experimental study of permeability development as a function of crystal-free melt viscosity. Earth Planet. Sci. Lett. 435, 45–54. http://dx.doi.org/10.1016/j.epsl.2015.11.035.

Lindquist, W.B., Lee, S.-M., Coker, D.A., Jones, K.W., Spanne, P., 1996. Media axis analysis of void structure in three-dimensional tomographic images of porous media. J. Geophys. Res. 101, 8297–8310. http://dx.doi.org/10.1029/95JB03039.

Mancini, S., Forestier-Coste, L., Burgisser, A., James, F., Castro, J., 2016. An expansion–coalescence model to track gas bubble populations in magmas. J. Volcanol. Geotherm. Res. 313, 44–58. http://dx.doi.org/10.1016/j.jvolgeores.2016.01.016.

Martel, C., Iacono-Marziano, G., 2015. Timescales of bubble coalescence, outgassing, and foam collapse in decompressed rhyolitic melts. Earth Planet. Sci. Lett. 412, 173–185. http://dx.doi.org/10.1016/j.epsl.2014.12.010.

Mueller, S., Melnik, O., Spieler, O., Scheu, B., Dingwell, D.B., 2005. Permeability and degassing of dome lavas undergoing rapid decompression: an experimental determination. Bull. Volcanol. 67, 526–538.

Namiki, A., Manga, M., 2008. Transition between fragmentation and permeable outgassing of low viscosity magmas. J. Volcanol. Geotherm. Res. 169, 48–60. http://dx.doi.org/10.1016/j.jvolgeores.2007.07.020.

Okumura, S., Nakamura, M., Takeuchi, S., Tsuchiyama, A., Nakano, T., Uesugi, K., 2009. Magma deformation may induce non-explosive volcanism via degassing through bubble networks. Earth Planet. Sci. Lett. 281, 267–274.

Okumura, S., Nakamura, M., Nakano, T., Uesugi, K., Tsuchiyama, A., 2012. Experimental constraints on permeable gas transport in crystalline silicic magmas. Contrib. Mineral. Petrol. 164, 493–501.

Okumura, S., Nakamura, M., Uesugi, T., Tsuchiyama, A., Fujioka, T., 2013. Coupled effect of magma degassing and rheology on silicic volcanism. Earth Planet. Sci. Lett. 362, 163–170.

Polacci, M., Baker, D.R., La Rue, A., Mancini, L., Allard, P., 2012. Degassing behaviour of vesiculated basaltic magmas: an example from Ambrym volcano, Vanuatu Arc. J. Volcanol. Geotherm. Res. 233–234, 55–64. http://dx.doi.org/10.1016/j.jvolgeores.2012.04.019.

Polacci, M., Bouvet de Maisonneuve, C., Giordano, D., Piochi, M., Mancini, L., Degruyter, W., Bachmann, O., 2014. Permeability measurements of Campi Flegrei pyroclastic products: an example from the Campanian Ignimbrite and Monte Nuovo eruptions. J. Volcanol. Geotherm. Res. 272, 16–22.

Rust, A.C., Manga, M., Cashman, K.V., 2003. Determining flow type, shear rate and shear stress in magmas from bubble shapes and orientations. J. Volcanol. Geotherm. Res. 122, 111–132. http://dx.doi.org/10.1016/S0377-0273(02)00487-0.

Rust, A.C., Cashman, K.V., 2004. Permeability of vesicular silicic magma: inertial and hysteresis effects. Earth Planet. Sci. Lett. 228, 93–107.

Rust, A.C., Cashman, K.V., 2011. Permeability controls on expansion and size distributions of pyroclasts. J. Geophys. Res. 116.

Ruth, D., Ma, H., 1992. On the derivation of the Forchheimer equation by means of the averaging theorem. Transp. Porous Media 7, 255–264.

Saar, M.O., Manga, M., 1999. Permeability–porosity relationship in vesicular basalts. Geophys. Res. Lett. 26, 111–114.

Sahini, M., Sahimi, M., 1994. Applications of Percolation Theory. CRC Press.

Song, S.-R., Jones, K.W., Lindquist, W.B., Dowd, B.A., Sahagian, D.L., 2001. Synchrotron X-ray computed microtomography: studies on vesiculated basaltic rocks. Bull. Volcanol. 63, 252–263.

Takeuchi, S., Tomiya, A., Shinohara, H., 2009. Degassing conditions for permeable silicic magmas: implications from decompression experiments with constant rates. Earth Planet. Sci. Lett. 283, 101–110.

Wright, H.M.N., Roberts, J.J., Cashman, K.V., 2006. Permeability of anisotropic tube pumice: model calculations and measurements. Geophys. Res. Lett. 33.

Wright, H.M.N., Cashman, K.V., Rosi, M., Cioni, R., 2007. Breadcrust bombs as indicators of Vulcanian eruption dynamics at Guagua Pichincha volcano, Ecuador. Bull. Volcanol. 69, 281–300.

Wright, H.M.N., Cashman, K.V., Gottesfeld, E.H., Roberts, J.J., 2009. Pore structure of volcanic clasts: measurements of permeability and electrical conductivity. Earth Planet. Sci. Lett. 280, 93–104.

Yokoyama, T., Takeuchi, S., 2009. Porosimetry of vesicular volcanic products by a water-expulsion method and the relationship of pore characteristics to permeability. J. Geophys. Res. 114.

Yoshida, S., Koyaguchi, T., 1999. A new regime of volcanic eruption due to the relative motion between liquid and gas. J. Volcanol. Geotherm. Res. 89, 303–315.